Supporting Information

Ailianou et al. 10.1073/pnas.1602311113

Estimating the Strain Imposed on a U Crest During Crimping

The strain field imposed during crimping can be visualized by considering lines of material points on the outer diameter surface that are equally spaced along z, and on the outer bend surface that are equally spaced along r on an as-cut U crest before deformation (Fig. S1*A*, *Left*). Crimping places the inner bend (IB) of the U crest under compression and the outer bend (OB) under tension. The compressive forces create a bulge at the IB, distorting the spacing of material points in the θ–z plane and along the r direction (Fig. S1*A*, *Right*).

Neglecting any changes due to crystallization (the density difference between the crystalline and amorphous phases is less than 3%) (42), incompressibility can be applied to estimate the dimensions of the volume element in the crimped state (Fig. S1*B*, *Right*). That is, the tensile forces at the OB cause material points to move apart in the θ direction (Fig. S1*A*, *Right*) with a concomitant decrease in the spacing of points on the OB surface along the r direction (Fig. S1*A*, *Right*). The magnitude of the strain in the r direction can be estimated from SEM images that show crimping increases the thickness at the IB to 180 μm (~20% elongation in the r direction relative to the uniform 150-μm thickness of the as-cut scaffold) and decreases the thickness at the OB to 100 μm (~33% compression in the r direction relative to the initial 150-μm thickness). The tensile stresses along the θ direction during crimping tend to elongate the material in the θ direction; this elongation is in the range from ~50% (if there is no strain in the z direction, as illustrated in Fig. S1 *A* and *B*, *Right*) to 100% (if the strain in z equals that observed in the r direction). It is this elongation in the θ direction that drives the orientation of PLLA chains near the OB of a U crest, evident in polarized light micrographs and diffraction patterns (Fig. S5*F*).

Mechanical Characterization of Poly (L-lactide) Vascular Scaffolds

To explore a range of hoop elongations and axial elongations, pure PLLA was extruded into preforms with their dimensions selected to give identical final diameter and thickness when blow-molded to an expanded tube (3.5 mm OD, 150 μm thickness). The hoop elongation was varied mainly by the choice of the preform radius, and the axial elongation was varied by the axial displacement imposed during blow-molding/tube expansion (Table S1 and Fig. S2). The expanded tubes were then laser-cut either into specimens for tensile measurements (both for hoop direction and for axial direction) or into scaffolds that were crimped and deployed in identical conditions to examine the effect of processing history on scaffold performance (43).

Deformation in Metal Stents Compared with PLLA Scaffolds

Metals and polymers are subjected to tube-forming and laser-cutting to create as-cut stents and scaffolds, which can be crimped for deployment in coronary arteries. Despite the similarities in processing, the resulting morphology of deployed metal stents and PLLA scaffolds is dramatically different. As-cut metal stents are obtained by laser-cutting a pattern of struts onto tubes of the respective metal alloy (e.g., Co–Cr, stainless steel, and Mg). It is possible to directly obtain as-cut PLLA scaffolds from extruded tubes, but it is not desirable. Extruded PLLA tubes are mostly amorphous and have polymer chains aligned along the z direction, which results in poor hoop strength. As a result, PLLA preforms made from extruded tubes are first expanded to the arterial dimensions and then laser-cut. The process of tube expansion results in oriented crystallization and preferential alignment of PLLA chains along the circumference, which enhances hoop strength in the PLLA scaffold.

The as-cut stents and scaffolds are subsequently crimped, which places the inner bends of U crests under compression and the outer bends under tension. At first, it appears that crimping should weaken the material, which is true for metal stents but not for PLLA scaffolds. Reports in the literature indicate reduced mechanical properties for crimped metal stents in comparison with uncrimped metal stents (44). In PLLA scaffolds, the material at the inner bend plastically deforms and protrudes along the r direction to form bulges, which have no counterpart in metal stents (Fig. S3 *A* and *B*, *i*). Near the outer bend, elongation of material augments chain orientation (Fig. 3), which enhances tensile strength of the PLLA scaffold. The formation of diamond-shaped voids upon deployment is closely associated with the semicrystalline morphology and orientation of chains in polymers; diamond-shaped voids are not observed in metal stents (Fig. S3 *A* and *B*, *iii*). Unlike metal stents, the multiplicity of morphologies in crimped PLLA scaffolds plays a central role in increasing scaffold strength and enabling deployment without fracture.

Aligning and Mounting 15-μm-Thick Microtomed Sections for Microdiffraction Experiments

To perform linear scans along selected lines across a sample (here from the inner bend to the outer bend of a U crest; Fig. S4*A*), it is necessary to properly orient the sample with respect to the translation apparatus at the beamline. Embedding medium around a microtomed sample stabilizes its shape (e.g., preventing the sample from rolling into a scroll) and facilitates holding the sample in place. However, when the sample was mounted on the beamline (APS beamline 2-ID-D), only an X-ray camera was available, which cannot discriminate between the embedding medium and the scaffold, which have similar electron density. Therefore, we mount the sections in a specific orientation and position in a frame that can be quickly and properly oriented and positioned in the beam. Specifically, thin sections of the embedded scaffold (in the crimped and deployed state) were placed between two 1-μm-thick silicon nitride membranes supported on silicon frames (window size 2.0 mm × 2.0 mm, Norcada NX5200F). To facilitate alignment of samples for microdiffration line scans along the z direction and θ direction, the specimens were oriented such that the z and θ axes were parallel to edges of the silicon frame (Fig. S4*B*). Inspection using polarized light showed that the sections did not move during transport. The boundary between the silicon frame and the silicon nitride membrane was readily identified using the X-ray camera (e.g., Fig. S4*B*, white + marks). The positions of selected points on the specimen relative to the frame (measured using a polarized light microscope) were used to specify the coordinates of points at which to begin and end a line scan of X-ray microdiffraction measurements (e.g., Fig. S4*B*, black + marks on the inner and outer bend of the U crest of section C45 described in Fig. 3).

X-ray beam damage is always a concern with polymers, particularly when the specimen is only 15 μm thick. Therefore, we acquired pairs of wide-angle X-ray scattering patterns using two sequential 30-s exposures. The difference between the two scattering patterns was used to quantify the extent of beam damage. Relative to the first of the two acquisitions, the second acquisition showed a reduction of intensity of ~20% at the (110/200) diffraction. This difference was sufficiently small that we chose to use sum of the two acquisitions to maximize signal-to-noise ratio in the scattering pattern analyzed for each measurement point. The second X-ray exposure was also used

to produce a slight, yet visible burn mark that provided a record of the exact position where the scattering pattern was measured.

Extreme Structural Anisotropy in a Crimped U Crest

Diffraction patterns were acquired in 5-μm steps from the IB to the OB of a crimped U crest (C45; Fig. S5*A*). Near the IB (Fig. S5 *B–D*), a broad azimuthal distribution (Fig. S5*G*) of (110)/(200) diffraction peaks indicates PLLA chains tilting out of plane (along the r direction). Toward the OB (Fig. S5 *E* and *F*), a steady and sharp decrease in the azimuthal width of (110)/(200) diffraction peaks confirms a highly oriented structure (along the θ direction). The crimped state displays dramatic variations in morphology on the micrometer scale.

Structural Homogeneity in a Deployed U Crest

The highly anisotropic crimped microstructure is transformed during deployment. Diffraction patterns from the IB to the OB (acquired in 5-μm intervals) of section D40 (Fig. S6*A*) are extremely similar (Fig. S6 *B–D*), suggesting a highly uniform structure. The narrow azimuthal width (~10°) (Fig. S6*E*) of the (110)/(200) diffraction peaks indicates a high degree of orientation (along the θ direction) in the deployed scaffold.

X-Ray Microdiffraction Data Analysis

Microdiffraction experiments were performed using 15-μm-thick sections of the polymer PLLA (beamline 2-ID-D, 200-nm spot size, APS, Argonne National Laboratory). Due to the small thickness of the sample, the scattering intensity from the PLLA sections is a mere 6% above the background (Fig. S7). Over the course of the 72 h of microdiffraction beamtime, the background varied in excess of 10% (Fig. S8), making it difficult to isolate the scattering due to the thin PLLA section.

To properly account for variations in background intensity, we studied 20 background patterns measured with the same acquisition time that was used for the samples (30 s), at intervals of between 1 min and 8 h over the course of 40 h of beamtime. The 20 background patterns do not superimpose, and the variations at low q ($0.5 < q < 0.55$ Å^{-1}) are much greater (~17%) than the variations (~8.5%) at high q ($2.7 < q < 2.8$ Å^{-1}) (Fig. S8). Thus, the background changes in shape as well as intensity. The beam intensity was recorded with every acquisition. The average intensity at high q ($2.7 < q < 2.8$ Å^{-1}) approximately tracks the beam intensity, but not exactly. Therefore, the conventional method of background subtraction (normalizing by the beam intensity recorded with each acquisition) is not appropriate. The presence of a high-q interval ($2.7 < q < 2.8$ Å^{-1}) in which the PLLA contribution is negligible offers the option of using the average intensity at high-q as an internal standard for the beam intensity (Fig. S9). The remaining variations of the background at low q are, however, comparable to the total number of counts due to a 15-μm-thick PLLA section (the scale used in Fig. S9*B* corresponds to the maximum signal contributed by a 15-μm PLLA section in a single 30-s acquisition).

The background residuals have a very consistent shape (Fig. S9) that matches the shape of the background patterns as a whole (Fig. S8), consistent with the hypothesis that the additional effect (beyond the effect of beam intensity) is likely due to small variations in the air, e.g., pressure or humidity. In turn, this suggests a two-parameter background subtraction method. We take advantage of the fact that the scattering due to background plus PLLA is indistinguishable from the background at both the low-q and high-q limits of the experimentally accessible q range (black rectangles in Fig. S7). Therefore, each scattering pattern contains sufficient information to compute two parameters that capture the ~17% variations in the magnitude of the air scattering (the difference between the low-q and high-q intensity, ΔI) and the small variations in the high-q intensity, I_h. We test a simple two-parameter background subtraction method in which the background pattern is scaled to accord with the sample's ΔI, and then a small offset is applied to match the sample's I_h. If the scattered intensity for background plus sample is denoted $S(q,\Phi)$ and that of the background is $B(q,\Phi)$, then

$$S(q,\Phi)_{\text{subtracted}} = S(q,\Phi) - \alpha B(q,\Phi) - \beta, \qquad \textbf{[S1]}$$

where $\alpha = \Delta I_S/\Delta I_B$ and $\beta = I_{h,S} - \alpha I_{h,B}$ with the subscript denoting the pattern $i = S$ or B for which the quantity ΔI_i or $I_{h,i}$ is evaluated. The method is applied to 2D datasets; for illustration, the azimuthally averaged plots, $I(q)$, are shown for a pair of $S(q,\Phi)$ and $B(q,\Phi)$ in Fig. S10*A* and for $S(q,\Phi)$ and $\alpha B(q,\Phi) + \beta$ in Fig. S10*B*. To test the ability of this method to precisely null-out variations in the background, we used the two groups of background patterns described above (Figs. S8 and S9), patterns 1–14 before the synchrotron beam going down and 15–20 afterward. The average of the patterns in a group was used as the $B(q,\Phi)$ for that group. For a particular background pattern, $S(q,\Phi)$ intensities at low q ($0.5 < q < 0.55$ Å^{-1}) and high q ($2.7 < q < 2.8$ Å^{-1}) were evaluated for each pattern, and pixel by pixel, $\alpha B(q,\Phi) + \beta$ was subtracted from $S(q,\Phi)$. The residuals are shown in Fig. S11 using the same scale as Fig. S9, for which the maximum signal contributed by a single 30-s acquisition of a PLLA thin section is 10. The residual is consistently less than ±1 (Fig. S12), i.e., less than 5% of the PLLA signal (residual <0.5% of background).

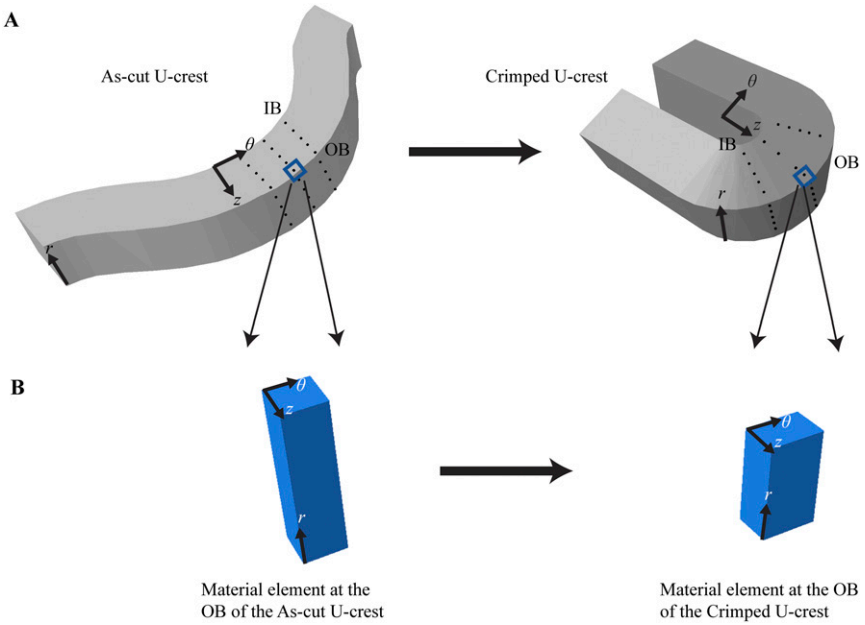

Fig. S1. Estimating the strain field created during crimping. (*A*) Visualizing the strain field with an array of material points (black dots). (*Left*) As-cut U crest. (*Right*) Crimped U crest. (*B*) Estimating the elongation at the OB along the θ direction. (*Left*) An infinitesimally small volume element at the OB of the as-cut scaffold. (*Right*) The same volume element in the crimped state, here illustrated with the *z* dimension unchanged and showing that the *r* dimension decreases by 33% during crimping (based on unpublished SEM images).

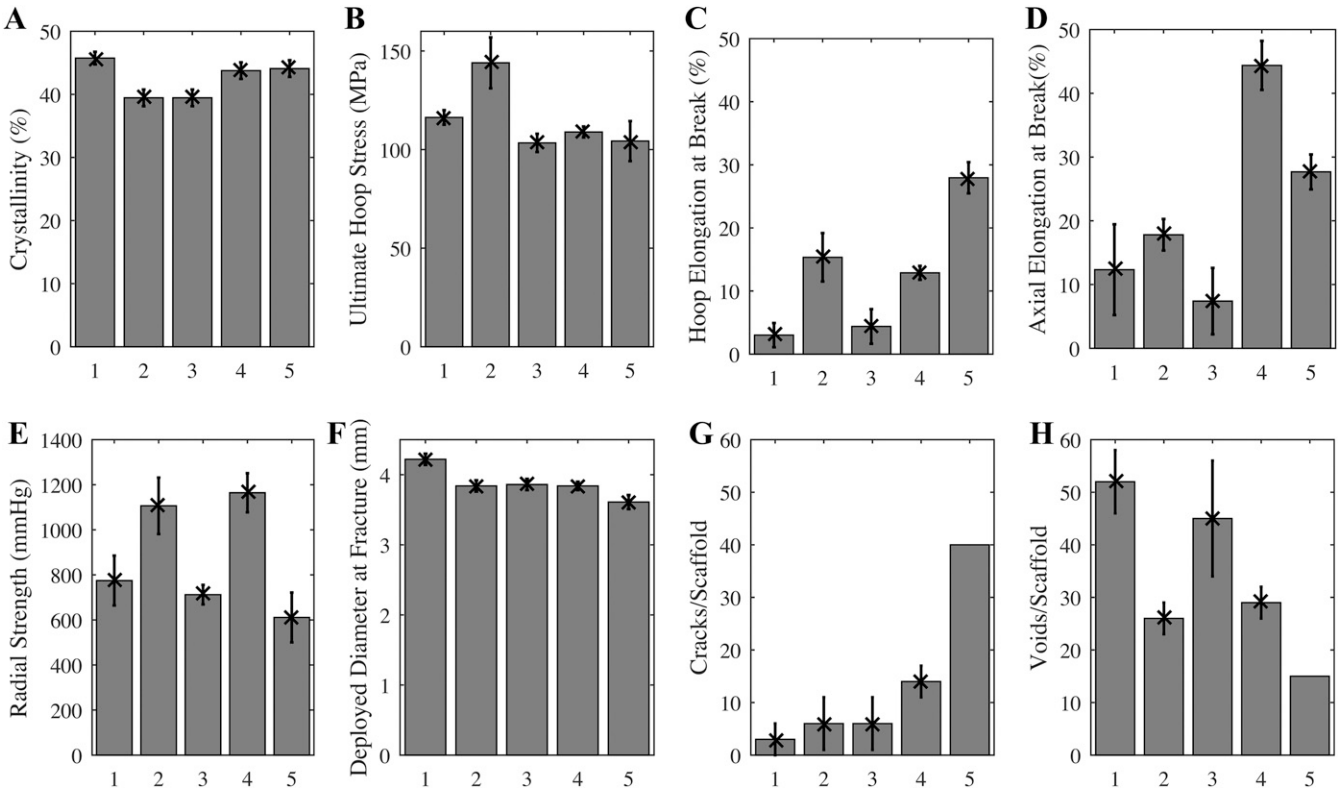

Fig. S2. Mechanical properties of expanded tubes (*A*–*D*) and deployed scaffolds (*E*–*H*) for groups given in Table S1. Apparent crystallinity (*A*) inferred from DSC thermograms ($n = 15$). Ultimate stress at fracture (*B*) and the elongation at break (*C*) for notched dog bone specimens laser-cut with long axis of the dog bone oriented along the hoop direction of the expanded tube ($n = 15$). Elongation at break (*D*) for notched dog bone specimens laser-cut with long axis of the dog bone oriented along the axial direction of the expanded tube ($n = 15$). Crimped scaffolds made from expanded tubes using identical laser-cutting and crimping conditions were tested to failure upon deployment. The radial strength (*E*) of scaffolds deployed to 3.5-mm diameter ($n = 5$) is measured under a compressive radial load that is increased until fracture occurs (MSI RX650 Radial Force Testing Instrument). Scaffolds were deliberately overdilated to evaluate the deployed diameter at fracture (*F*, $n = 5$). For specimens that survive to a deployed diameter greater than that of the expanded tube (3.5 mm), the number of cracks (*G*) and diamond-shaped voids (*H*) are presented ($n = 5$, except for group 5, for which only one scaffold survived to 3.5-mm diameter, so 40 represents a lower bound on cracks/scaffold). In addition to coauthors M.B.K. and J.P.O., the following Abbott technologists contributed to these experiments: Thierry Glauser, Vincent Gueriguian, Bethany Steichen, Manish Gada, and Lothar Kleiner. Figure adapted from ref. 43.

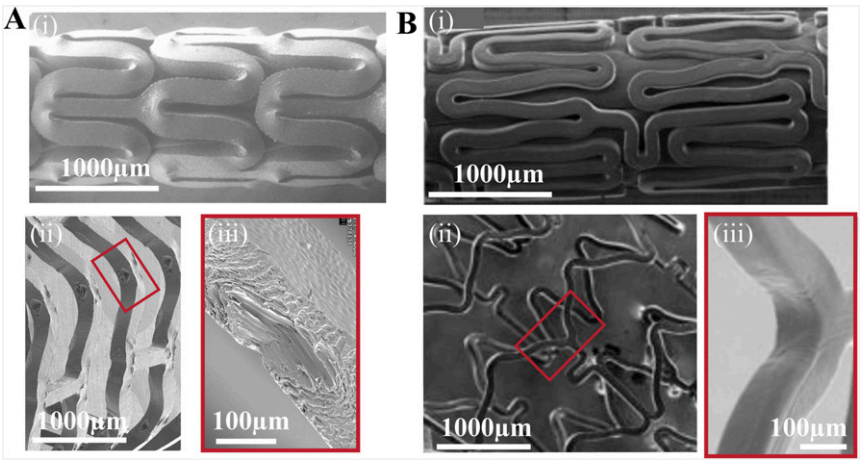

Fig. S3. Influence of material properties on the crimped and deployed state of vascular implants. Scanning electron microscopy is used to compare a 150-µm PLLA scaffold (*A*) and an 80-µm cobalt–chromium (*B*) permanent stent (45, 46). The PLLA scaffold and Co–Cr stent are crimped (*A and B*, *i*) onto a balloon catheter and deployed (*A and B*, *ii*) to an outer diameter of 3.5 mm. The inner bends of deployed struts (*A and B*, *iii*) indicate that diamond-shaped voids are specific to PLLA scaffolds. [Fig. S3*B, i–ii* is reprinted with permission from ref. 45, and Fig. S3*B, iii* is reprinted with permission from ref. 46.]

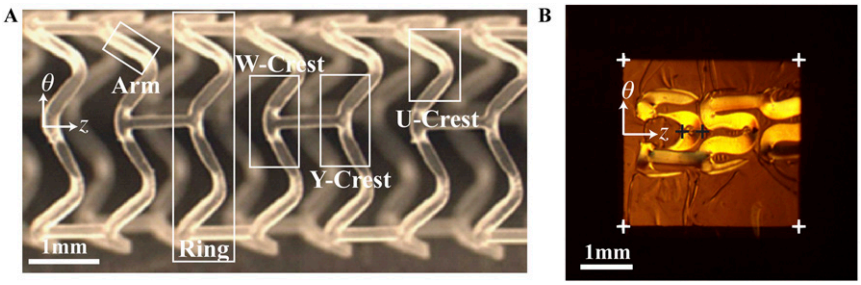

Fig. S4. Definition of terms and illustration of the part of the sample that was embedded in preparation for microtoming sections. (*A*) The scaffold is laser-cut to remove most of the material of the expanded PLLA tube, leaving the rings and struts that make up the scaffold. We chose to examine U crests because they capture the intense, local deformation that occurs during crimping (whereas the arms mainly reorient without deforming and struts neither reorient nor deform). The outline (34) indicates the typical size and orientation of the embedded specimen from which sections were cut. Fig. S4*A* reprinted with permission from ref. 34. (*B*) A section cut from a crimped scaffold (specifically C45; Figs. 2*B* and 3).

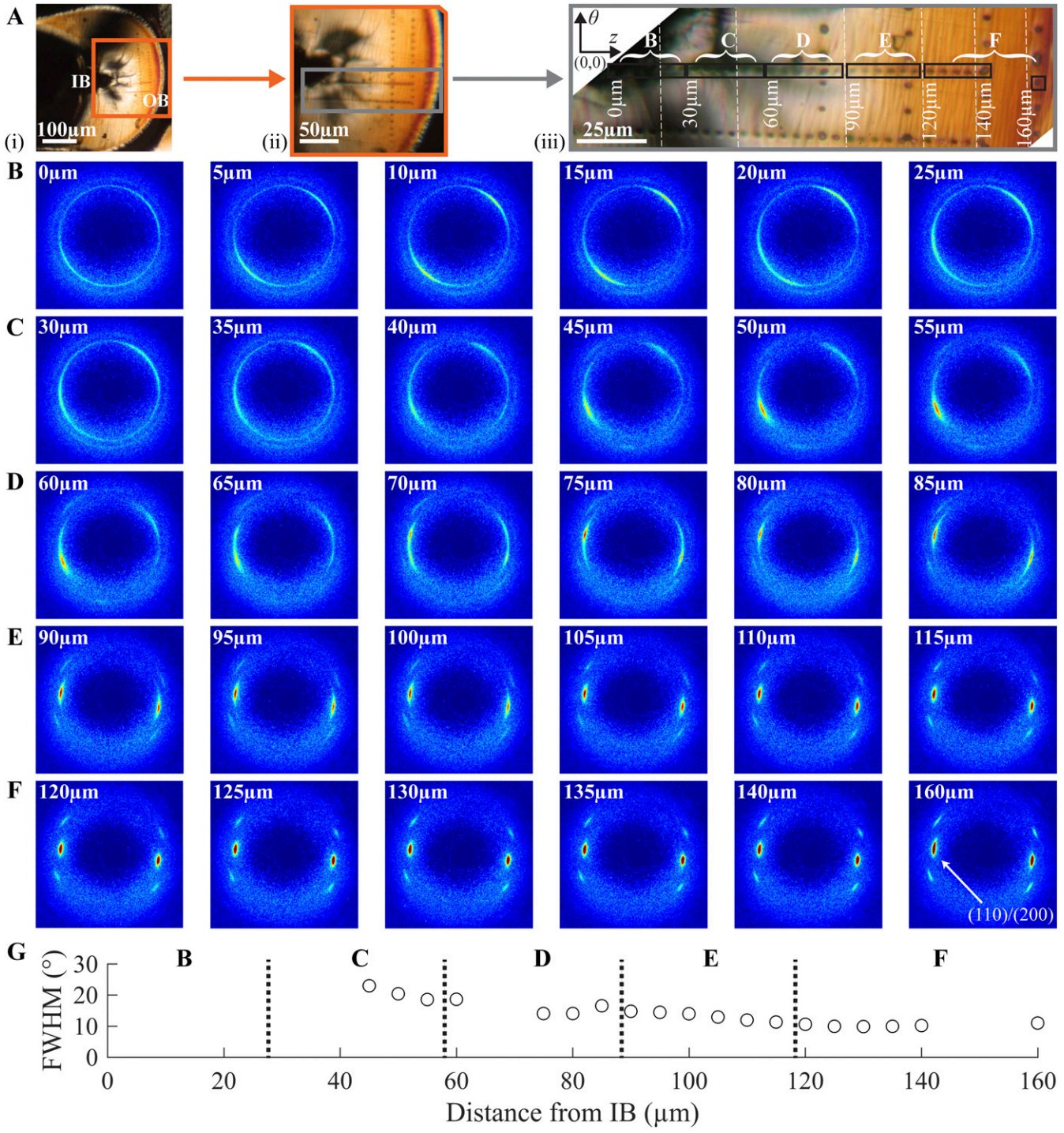

Fig. S5. Variation in morphology from the inner bend (IB) to the outer bend (OB) of the C45 crimped U section. (*A*) Polarized light images of the C45 crimped section (higher magnification image comprises multiple images stitched together at vertical white dashed lines). (*B*–*F*) Diffraction patterns acquired at the positions of the corresponding burn marks in *A*. The (110)/(200) peaks are indicated in *F* (160 μm). (*G*) The azimuthal full width at half maximum (FWHM) for the (110)/(200) peaks of the diffraction patterns serves as a measure of the strength of orientation of the crystallites. Note that values are not given for patterns acquired near the IB, where the polymer chains tilt out of plane and the azimuthal spread becomes increasingly broad (*B* and *C*), making it difficult to identify distinct peaks.

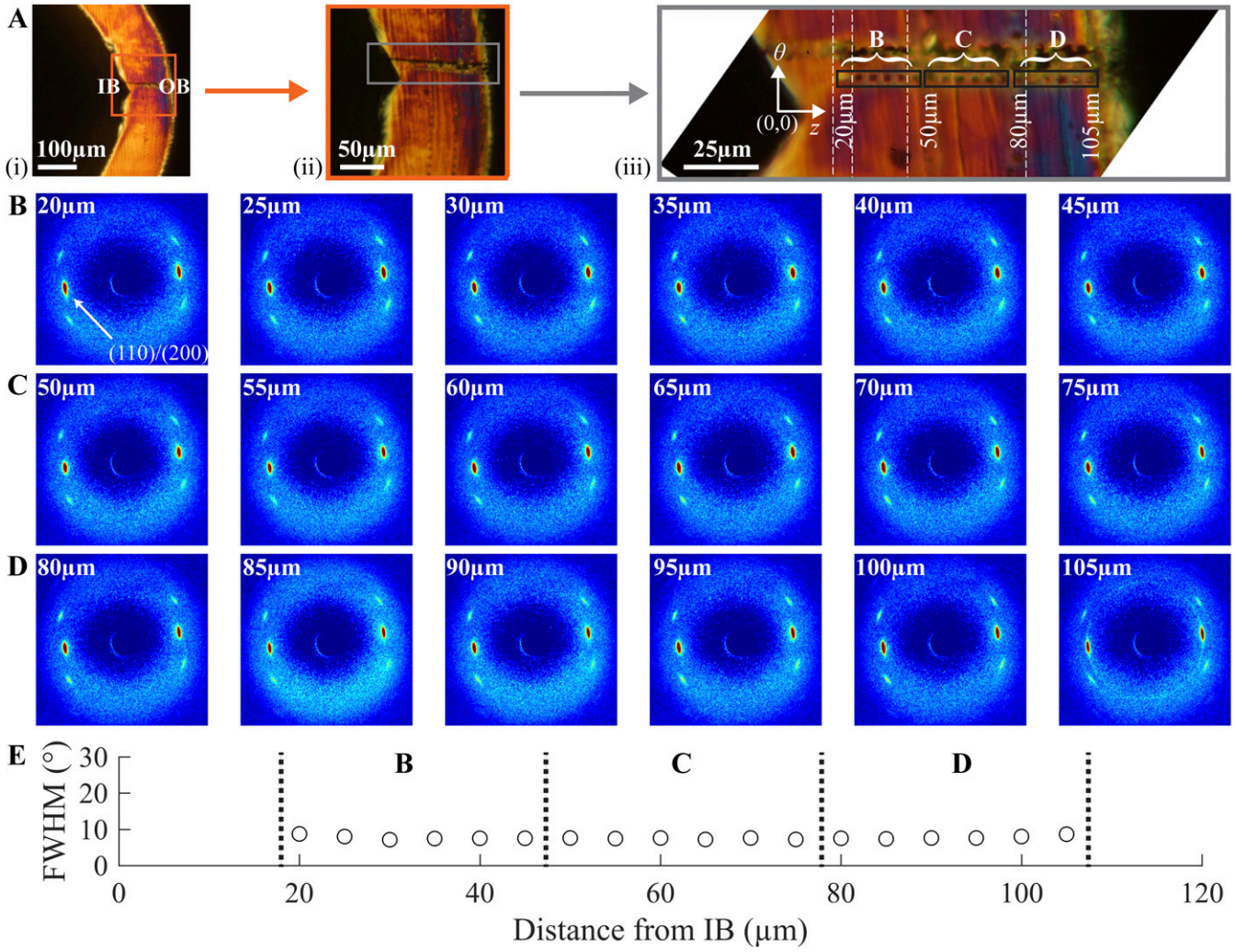

Fig. S6. Variation in morphology from the inner bend (IB) to the outer bend (OB) of the D40 deployed U section. (*A*) Polarized light images of the D40 deployed section (higher magnification image comprises multiple images stitched together at vertical white dashed lines). (*B–D*) Diffraction patterns acquired at the positions of the corresponding burn marks in *A*. The (110)/(200) peaks are indicated in *B* (20μm). (*E*) The azimuthal FWHM for the (110)/(200) peaks of the diffraction patterns serves as a measure of the strength of orientation of the crystallites.

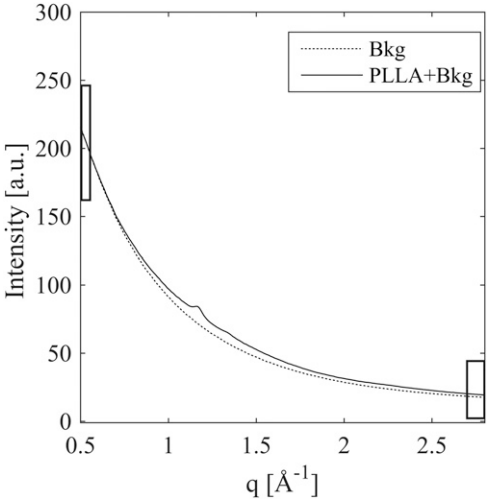

Fig. S7. Background scattering (dashed) compared with background plus a 15-μm-thick section of poly(L-lactide) (solid). The background and the sample scattering were acquired within 7 min of each other using a 30-s acquisition. The greatest difference between the two is at the (110)/(200) diffraction peak (less than 10%), and the PLLA contribution is negligible at both low-q ($0.5 < q < 0.55$ Å^{-1}) and high-q ($2.7 < q < 2.8$ Å^{-1}), indicated by black rectangles.

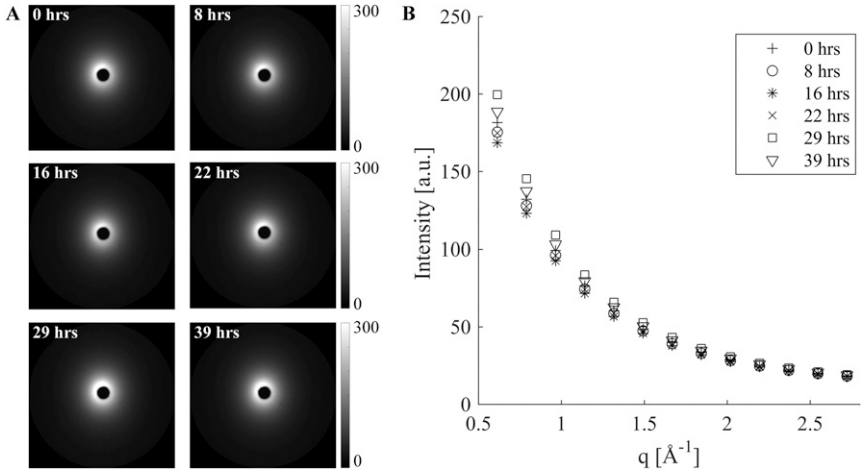

Fig. S8. Variation in background scattering. Representative background scattering patterns acquired over a period of 39 h presented as (*A*) 2D images and (*B*) azimuthally averaged *I*(*q*) plots.

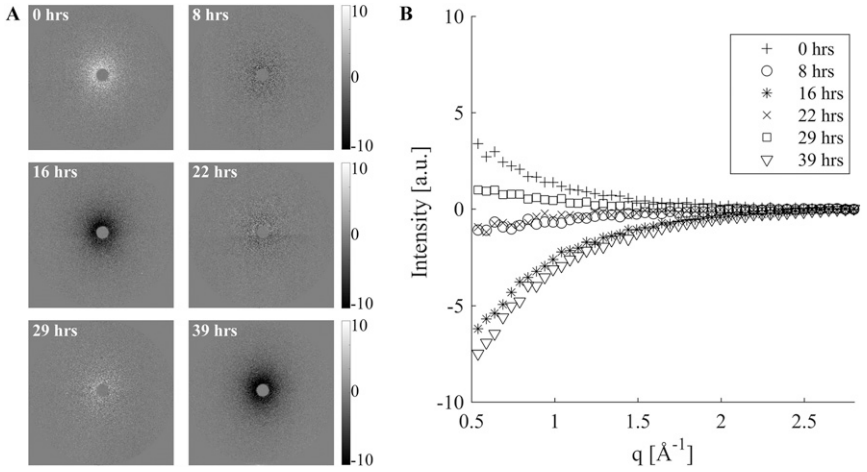

Fig. S9. Deviation among background patterns at low *q*, despite using an internal standard for beam intensity presented as (*A*) 2D images and (B) azimuthally averaged *I*(*q*). Background patterns (Fig. S8) were analyzed in two groups (1–14 before the synchrotron beam going down and 15–20 afterward). The average of the patterns in a group was used as the background for that group. Normalization by the intensity in the *q* range 2.7–2.8 Å^{-1} before subtraction produced a near-zero residual only for $q > 2.4$ Å^{-1}; at low *q*, the residual varied from +2% to −4% of the overall background. Relative to the maximum signal contributed by a single 30-s acquisition of a 15-μm PLLA section (its 110/200 peak), the low-*q* residual ranges from −40% to +25%, swamping out the variations among the PLLA patterns.

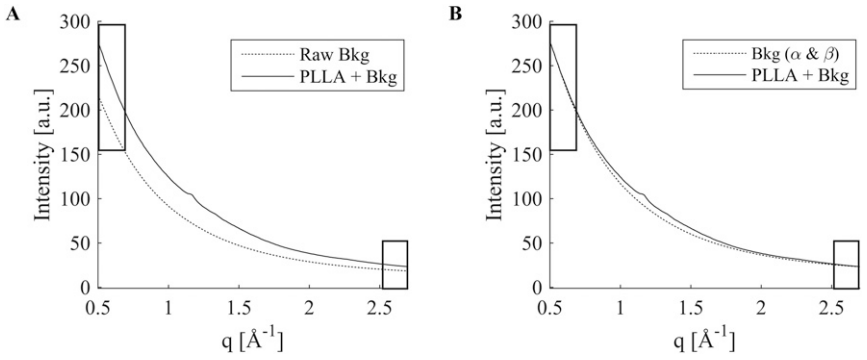

Fig. S10. Schematic illustration of two-parameter background subtraction. (*A*) When the average of background patterns (Raw Bkg) is subtracted from the sample diffraction pattern (PLLA + Bkg), large disparities at *q* values at which sample plus background is known to be indistinguishable from the background [marked by rectangles (compare Fig. S7)] are observed. This disparity cannot be removed with simple scaling (Fig. S9). (*B*) The disparity can be removed by a two-parameter adjustment $\alpha B(q, \Phi) + \beta$ of the background [Bkg(α & β)] (see Eq. **S1** and text for formulae for α and β).

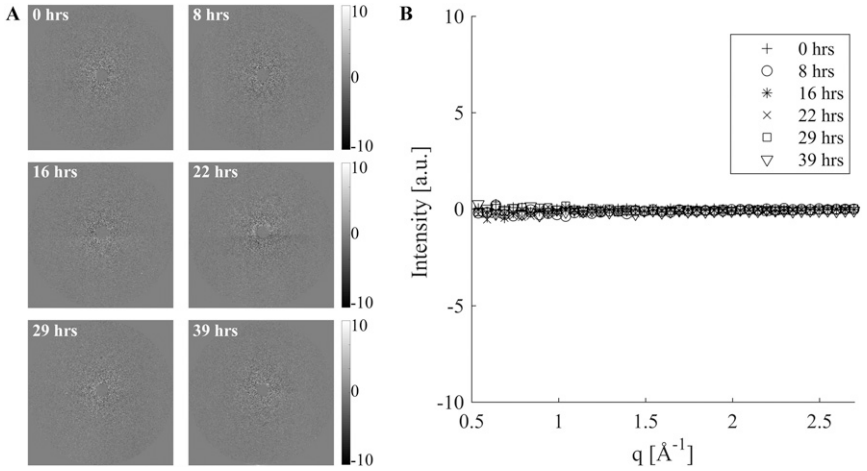

Fig. S11. Validation of two-parameter background subtraction, for the same sets of background scattering patterns as in Fig. S8 and again using the average of the patterns in a group as the background $B(q, \Phi)$ for that group. The residuals after subtraction of $\alpha B(q, \Phi) + \beta$ (see text for formulae for α and β) from representative individual background patterns are shown (*A*) as 2D images and (*B*) as azimuthally averaged $I(q)$.

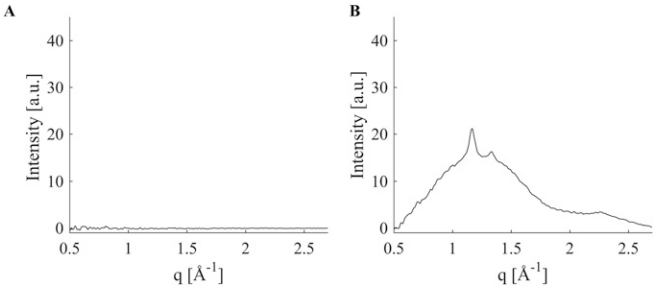

Fig. S12. Effect of two-parameter background subtraction on PLLA intensity. Comparison of (*A*) the residual of a representative two-parameter subtraction of one background dataset from another and (*B*) the signal due to PLLA (from two 30-s acquisitions) isolated using two-parameter background subtraction.

Table S1. Expanded PLLA tubes, grouped by the axial and radial deformation during tube expansion

Group	Extruded ID, mm	Extruded OD, mm	Expanded ID, mm	Expanded OD, mm	OD strain, %	ID strain, %	Axial strain, %
1	0.53	1.65	3.20	3.50	112	500	20
2	0.53	2.53	3.20	3.50	38	500	200
3	0.64	1.69	3.20	3.50	107	400	20
4	0.80	2.17	3.20	3.50	61	300	100
5	1.07	2.69	3.20	3.50	30	200	200